IEEE Access
Multidisciplinary ⋮ Rapid Review ⋮ Open Access Journal

Received 14 April 2023, accepted 3 May 2023, date of publication 10 May 2023, date of current version 17 May 2023.

Digital Object Identifier 10.1109/ACCESS.2023.3274840

RESEARCH ARTICLE

Facial Recognition in Hexagonal Domain–A Frontier Approach

TANER CEVIK[1], NAZIFE CEVIK[2], JAWAD RASHEED[3], (Member, IEEE), ADNAN M. ABU-MAHFOUZ[4,5], (Senior Member, IEEE), AND ONUR OSMAN[6]

[1]Software Engineering Department, Faculty of Engineering and Architecture, Istanbul Arel University, 34537 Istanbul, Turkey
[2]Computer Engineering Department, Faculty of Engineering and Architecture, Istanbul Arel University, 34537 Istanbul, Turkey
[3]Department of Software Engineering, İstanbul Nişantaşi University, 34398 Istanbul, Turkey
[4]Council for Scientific and Industrial Research (CSIR), Pretoria 0184, South Africa
[5]Department of Electrical and Electronic Engineering Science, University of Johannesburg, Johannesburg 2006, South Africa
[6]Department of Electrical and Electronic Engineering, İstanbul Topkapi University, 34087 Istanbul, Turkey

Corresponding author: Jawad Rasheed (jawad.rasheed@nisantasi.edu.tr)

ABSTRACT Many face-recognition (FR) methods have been proposed thus far. Although FR has achieved wisdom in square pixel-based image processing (SIP) due to many studies, this wisdom has not been transferred to Hexagonal pixel-based image processing (HIP) until now. This study presents HIP versions of the most basic texture extraction studies in SIP, namely Gray-Level-Co-occurrence-Matrices (GLCM), Local Binary Pattern (LBP), and our recent work, local-holistic graph-based descriptor (LHGPD). The images are first transformed from the SIP domain to the HIP domain. The HIP domain equivalences (HexGLCM, HexLBP, and HexLHGPD) of the SIP domain GLCM, LBP, and LHGPD are then established. Finally, the facial recognition performances of the SIP and HIP domain versions of GLCM, LBP, and LHGPD are evaluated and compared on the primary data sets. The results of the experiments reveal that HIP domain GLCM, LBP, and LHGPD show a par performance, surpassing them in places when compared to their counterparts in the SIP domain regarding face recognition accuracy.

INDEX TERMS Facial recognition, hexagonal image processing, hexel, classification.

I. INTRODUCTION

Facial data is one of the most popular and practical biometrics due to its strong discrimination performance and ability to be gathered in real-time by devices like cameras without physical touch or human interaction [1], [2], [3]. Due to its challenges and wide range of applications, autonomous face recognition, or facial recognition by a machine, continues to be a study subject that receives much interest. Although facial recognition has a variety of uses, such as in surveillance, computer-human interaction, and commercial and legal identification [4], the most frequent difficulties that make the process particularly challenging are variations in age, facial expression, exposure, lighting, and the presence of noise [5], [6], [7], [8].

Traditional object identification techniques are unlikely to be effective in face recognition, as there is a slight variation in the number of classes in object recognition. In contrast, the number of classes increases by adding a new person to the knowledge base in face recognition. Face recognition is a multi-class classification issue as a result. Therefore, recommended facial recognition techniques are desired to work in this complex environment [9].

Face representation and face matching are essential, even though face detection, face alignment, face representation, and face matching are the four fundamental processes of a typical face recognition system. Noise, occlusion, differences in expression, and lighting are frequently present in facial images taken in inaccessible settings, which significantly lowers discrimination performance by reducing the similarity between the images of the same person or making the images of different people look similar [10].

The two main categories of face representation techniques are holistic and local feature-based approaches [11], [12]. Holistic methods look at the entire image and consider the holistic aspects representing the overall face

The associate editor coordinating the review of this manuscript and approving it for publication was Peter Peer.

qualities [13]. The leading and influential representatives of the holistic branch, which sparked numerous additional studies [14], [15], are the Gray-level co-occurrence matrices (GLCM) [16], [17], principal component analysis (PCA) [18], [19], linear discriminant analysis (LDA) [17], independent component analysis (ICA) [20].

Local descriptor-based techniques, instead of holistic ones, concentrate on learning from specific local patterns in the picture. They can withstand challenges such as changes in light and facial expression better [21]. Numerous research projects have been carried out, including Local Tetra Patterns (LTetP) [22], Monogenic Binary Coding (MBC) [23], Local Monotonic Pattern (LMP) [24], Local Ternary Pattern (LTP) [25], Local Derivative Pattern (LDrvP) [26], Local Directional Pattern (LDP) [27], Local Transitional Pattern (LTrP) [28], Local Phase Quantization (LPQ) [29], Weber Local Descriptor (WLD) [30], Local Gradient Pattern (LGP) [31], Median Binary Pattern (MBP) [32], Local Arc Pattern (LAP) [33]) have been carried out, among which Texton Learning [34], [35], Local Binary Pattern (LBP) [36], Gabor wavelets [37], [38] and Radon transformations [39].

Converting human vision into computer vision is known as image processing. Specific sensors are utilized to gather continuous data in the physical light medium. These sensors offer a wide range of light sensitivity and are used in square or rectangular arrays. Even though light data is continuous, computers can only handle digital data. So, sampling and digitization of continuous light data are required. The use of rectangular or square sensor arrays impacts subsequent computer processing. Thus, the pixel—the smallest digital data unit in a computer system—is transformed into a square.

On the other hand, collecting light data on a hexagonal lattice and processing it as a hexagon domain may change many things and produce positive results. Hexagonal geometry has been studied for a long time. Hexagons were not the best way to divide a plane into equal-sized sections before Hales [40], [41] demonstrated that they were. In addition to the naturally hexagonal arrangement of photoreceptors in the fovea, honeycombs are another instance of hexagonal geometry in nature [42]. Compared to its square sibling, the hexagonal lattice construction has certain advantages. Better radial symmetry enables circular symmetric kernels, which improves detection accuracy for straight and curved edges and the homogeneity of the hexagonal lattice structure, which provides local equality and uniqueness [43].

A. CONTRIBUTIONS OF THIS STUDY

HIP has gotten little attention since it lacks the requisite hardware, algebraic, and software components to handle hexels. However, HIP must be appropriately scrutinized to see if it may help with the issue of data size and, therefore, processing time. Working with the HIP is particularly fascinating since it could improve the accuracy of typical SIP methods like edge detection, segmentation, and object recognition. Although face recognition has a long history in the SIP space, there has been little [44], [45], [46], [47], [48] to apply or advance it in the HIP space. The following is an expression of the contributions of this study:

- Not much work has been put into facial recognition for the HIP domain. The most fundamental texture extraction research in SIP—Gray-Level Co-occurrence Matrix (GLCM), Local Binary Pattern (LBP), and our most recent study, local-holistic graph-based descriptor (LHGPD)—are presented here in HIP variants.
- The simulation findings show that, in terms of discriminating accuracy, face recognition performed in the HIP is superior to face recognition performed in the SIP.

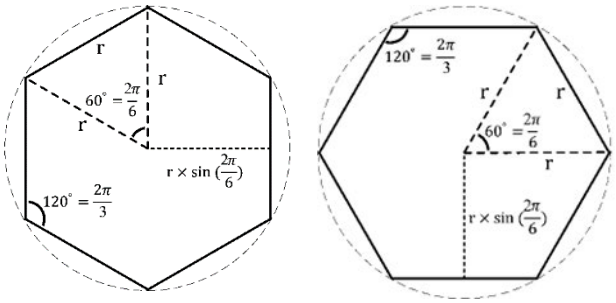

(a) Vertical hexel (b) Horizontal hexel

FIGURE 1. Hexels that are oriented vertically and horizontally.

B. ARTICLE OUTLINE

The remainder of the article is structured as follows. In Section II, the established hexagonal structure is introduced. The basics of the SIP domain GLCM, LBP, LHGPD, and their suggested HIP counterparts are addressed in Section III. In Section IV, the testing datasets and the experimental setup is clarified. Interpretations of the results are presented in Section V, while Section VI closes by summarizing our conclusions and possible directions for future research.

II. HIP INFRASTRUCTURE

Regular hexels, which correspond to the SIP definition of a pixel, are present in the pictures in the HIP domain. Hexels are a viable alternative for conveying visual information because of their distinctive features. Physical infrastructure functions best when intensity and color data are obtained from a camera sensor that supports hexels and shown on a monitor that supports hexels. When this essay was published, there were not many artifacts that were open to the public. As a result, we used mimic techniques to project pixels to hexels. Figure 1 displays hexels in both vertical and horizontal orientations. The horizontal and vertical layouts of the hexagonal tiling derive from these orientations.

Hexagonal patterns and their surrounding hexagons are impacted by hexagonal orientation. There are three axes with a $\pi/6$ difference on the six sides of a hexagon. Examples of tiled arrangements in horizontal and vertical orientations are shown in Figure 2. Two oblique axes in this investigation are

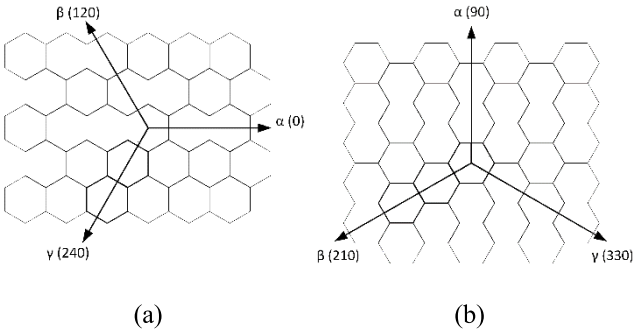

FIGURE 2. Orientations (a) vertical and (b) horizontal of the hexagonal layout's axes.

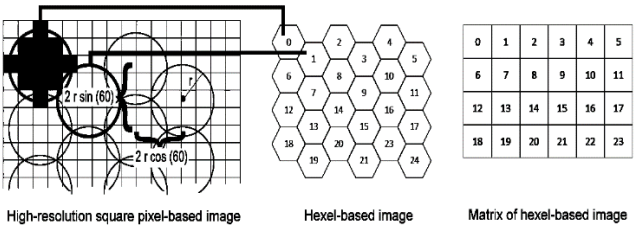

FIGURE 3. Using circular occupancy to convert a high-resolution square pixel-based image into a hexel-based image.

identified as β and γ. In addition, the α-axis indicates either the horizontal or vertical axis depending on the orientation of the hexels. The α axis is 0° for vertical hexels (Figure 2.a) and 90° (Figure 2.b) for horizontal hexels.

Hexagonal orientation affects hexagonal patterns and the hexagons that surround them. A hexagon has six sides and three axes with a difference of $\pi/6$. Figure 2 displays examples of tiled layouts in both horizontal and vertical orientations. In this inquiry, two oblique axes are designated as β and γ. Additionally, depending on how the hexagons are oriented, the α -axis denotes either the horizontal or vertical axis. Figure 2.a shows the axis at 0° for vertical hexagons, while Figure 2.b shows it at 90° for horizontal hexagons.

A. SIP TO HIP PROJECTION

It is significant to highlight that acquiring intensity data from a camera sensor with hexagonal support is ideal for hexagonal images. We employed two different methods to convert an image received as a square pixel from the SIP domain to the HIP domain due to the unavailability of such hardware. The first method, circular averaging, uses a circle-shaped band of pixels to determine the average intensity for each hexel. This method is accurate, but it uses more computing power. The representations of this strategy are shown in Figure 3.

The alternate averaging method determines the average intensities of two adjacent vertical pixels for even (alternative) columns and transfers odd columns to the output matrix. Even while it is speedier than the prior method, it is less accurate. This method also results in a HIP domain matrix the same size as the original SIP domain image. Figure 4 depicts the visual for this projection technique using a different column average.

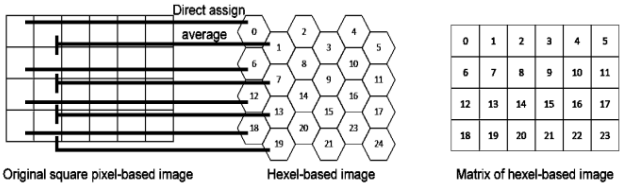

FIGURE 4. Transforming a SIP image into a HIP image using the mean of alternate columns.

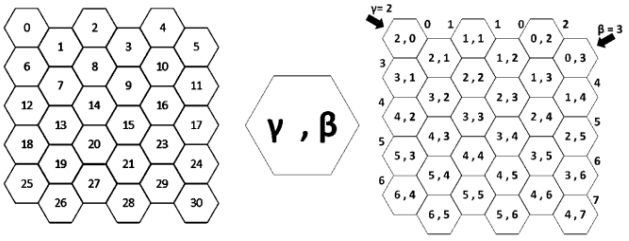

FIGURE 5. Hexagonal coordinates and indexing.

B. COORDINATES AND INDEXING

In contrast to pixel coordinates, hexagonal coordinates do not fit similarly. For pixels, the concept of a matrix works nicely. However, the lack of a proper data format hinders the hexels. This paper proposes a memory-friendly method for indexing and preserving the hexadecimal information of a picture. The neighbors of a hexagon must be determined using particular computations notwithstanding the infrastructure for storing hexagonal images in matrices. Figure 5 shows the coordinate and indexing data. The coordinate of the α-axis may be found by using the values of β and γ. As a result, the value is not stored by this technique. While the indexing begins in the upper right corner and travels leftward, that starts in the top left corner and moves down the right side.

The functions *HexelToIndex* and *IndexToHexel* convert a hexel's coordinate into an ordinary index and an ordinary index into a hexel's coordinate. In other words, these functions link a specific hexel's coordinate to its corresponding index in the storage matrix. The computations of the coordinates from Hexel to index and from index to Hexel are shown in Eq. (1-2).

$$\begin{aligned}
\gamma_T &= \left\lfloor w - \frac{(w+1)\,mod 2}{2} \right\rfloor \\
\gamma_S &= \begin{cases} (\gamma - \gamma_S) \times w & if\ \gamma > \gamma_T \\ (\gamma_S - \gamma) \times 2 & else \end{cases} \\
step &= \beta - |\gamma - \gamma_T| \\
index &= \max \begin{cases} (w+2) \times \left\lfloor \frac{step}{2} \right\rfloor + step\ mod 2 + \gamma_S \\ 2\beta - step \end{cases} \qquad (1) \\
r &= \left\lfloor \frac{index}{w} \right\rfloor \\
\gamma &= r + \left\lfloor \frac{w-1}{2} \right\rfloor - \left\lfloor \frac{index}{2} mod \frac{w}{2} \right\rfloor \\
\beta &= r + \left\lfloor \frac{index - r \times w + 1}{2} mod \frac{w+1}{2} \right\rfloor \qquad (2)
\end{aligned}$$

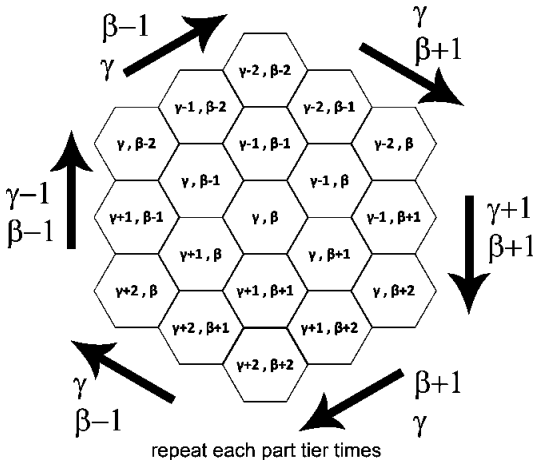

(a)

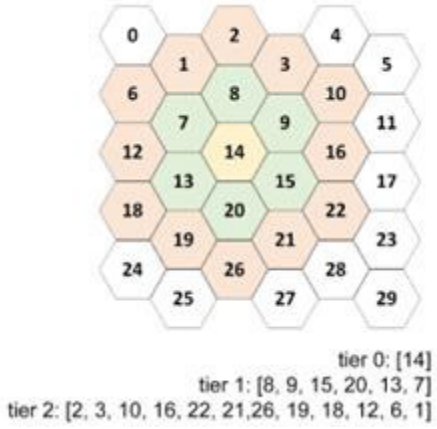

(b)

FIGURE 6. (a) Traverse mechanism (b) 3-tier-neighbors of a hexel.

C. TRAVERSING

The following process is the activity of traversing. The most basic tasks in image processing need the identification of a pixel's neighbors. Obtaining neighbors for a hexel is more complex than getting neighbors for pixels in traditional square matrices, especially for several layers. A specific method is developed that returns all of a hexel's neighbors for a specified set of tiers to obtain all of them swiftly. The traversal mechanism and three-tier neighbors of a hexagon are shown in Figure 6.

III. FACE RECOGNITION

This section comprehensively addresses the basics of the SIP domain GLCM, LBP, LHGPD, and their suggested HIP counterparts: HexGLCM, HexLBP, and HexLHGPD.

A. GLCM - HexGLCM

This section elaborates on one of the fundamental and earliest holistic methods, GLCM, and its hexagonal counterpart, HexGLCM. Firstly, a summarized explanation of GLCM is given, and following that, the proposed hexagonal counterpart, HexGLCM is explained in detail.

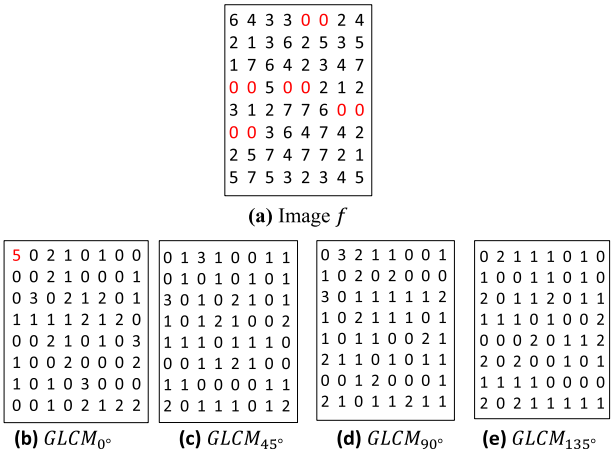

FIGURE 7. Demonstration of the GLCMs for a sample matrix.

1) GLCM

Haralick et al. suggested GLCM and several characteristics retrieved from these matrices for texture classification. The surrounding pixels (P_i, P_j), their intensity-relationships (R_{P_i,P_j}), and their frequency statistics are stored in GLCMs. The complete image is considered when computing the incidence statistics. As a result, it is categorized as a holistic approach. The following is the GLCM's operating logic: Let $f_{m\times n}$ be an image with m rows and n columns made up of pixels whose intensities range from 0 to $L-1$, where $0 < L \leq 256$, according to the operational logic of GLCM. The frequency of the pixel pair (P_i, P_j) occurring in f with orientation Q is shown by each GLCM element. The displacement vector $d = (dx, dy|dx = dy = dg)$ that is finally shown by the orientation represented by Q is the number of gaps (d_g) between the pixels of interest. $d_g = 0$ refers to the adjacency situation. The distance d_g between the pixel pairs (P_i, P_j) and the angle α can also be used to express orientation with two factors. α may have a value of 0°, 45°, 90°, or 135°. The values that d take theoretically rely on as follows: for $= 0° \rightarrow 0 \leq d_g \leq m-2$, $\alpha = 45° \rightarrow 0 \leq d_g \leq \min(m,n)$, $\alpha = 90° \rightarrow 0 \leq d_g \leq n-2$, $\alpha = 135° \rightarrow 0 \leq d_g \leq \min(m,n)$. For each image, four different GLCMs are created since there are four different angles: 0°, 45°, 90°, and 135°. Square matrices with equal sizes are GLCMs. The image's discrete intensity values, represented by the expression $GLCM_{L-1xL-1}$, determine their sizes. Figure 7 shows how to calculate four *GLCM*s for an example image $f_{8\times 8}$ whose pixel intensity values range from $[0-7]$: $GLCM_{0°}$, $GLCM_{45°}$, $GLCM_{90°}$, $GLCM_{135°}$.

After GLCMs have been calculated, Haralick characteristics are extracted from these. Table 1 lists the fourteen most well-known of them [48].

2) HEXGLCM

Due to the placement of hexels on a hexagonal grid differing from the square pixels' placement on a square grid, naturally, the orientation angles considered in GLCM also change.

TABLE 1. Haralick features.

Angular Second Moment	$f_1 = \sum_{i=1}^{N_g}\sum_{j=1}^{N_g} p(i,j)^2$
Contrast	$f_2 = \sum_{n=0}^{N_g-1} n^2 \left\{\sum_{i=1}^{N_g}\sum_{j=1}^{N_g} p(i,j)\right\}_{\lvert i-j\rvert=n}$
Correlation	$f_3 = \sum_{i=1}^{N_g}\sum_{j=1}^{N_g} \frac{(i-\mu_x)(i-\mu_y)(p(i,j)}{\sigma_x\sigma_y}$
Sum of Squares	$f_4 = \sum_{i=1}^{N_g}\sum_{j=1}^{N_g}(i-\mu)^2 p(i,j)$
Inverse Difference Moment	$f_5 = \sum_{i=1}^{N_g}\sum_{j=1}^{N_g} \frac{1}{1+(i-j)^2} p(i,j)$
Sum Average	$f_6 = \sum_{i=2}^{2N_g} i p_{x+y}(i)$
Sum Variance	$f_7 = \sum_{i=2}^{2N_g}(i-f_8)^2 p_{x+y}(i)$
Sum Entropy	$f_8 = -\sum_{i=2}^{2N_g} p_{x+y}(i)\log\{p_{x+y}(i)\}$
Entropy	$f_9 = -\sum_i \sum_j p(i,j)\log\{p(i,j)\}$
Difference Variance	$f_{10} = variance\ of\ p_{x-y}$
Difference Entropy	$f_{11} = -\sum_{i=2}^{N_g-1} p_{x-y}(i)\log\{p_{x-y}(i)\}$
Information Measures of Correlation	$f_{12} = \frac{HXY - HXY1}{max\{HX, HY\}}$ $f_{13} = (1-\exp[-2.0(HXY2-HXY)])^{1/2}$ $HXY = -\sum_i \sum_j p(i,j)\log p(i,j)$
Maximal Correlation Coefficient	$Q(i,j) = \sum_k \frac{p(i,k)p(j,k)}{p_x(i)p_y(k)}$ $f_{14} = (Second\ Largest\ Eigenvalue\ of\ Q)^{1/2}$

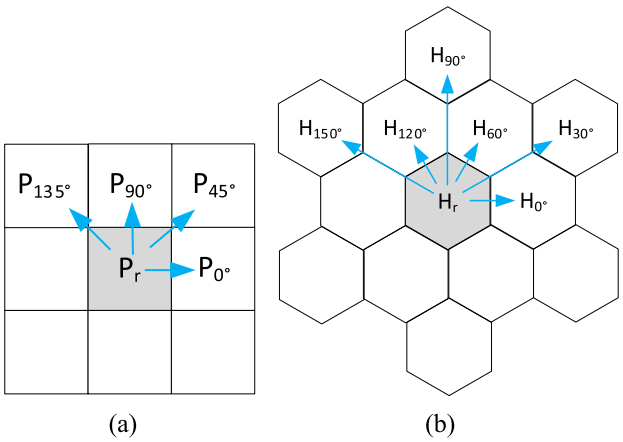

FIGURE 8. Angle-neighborhood orientation (a) GLCM (b) HexGLCM.

Rather than considering four angles, 0°, 45°, 90°, and 135°, as done in SIP domain, six angles, 0°, 30°, 60°, 90°, 120°, and 150°. Figure 8 illustrates the angle-neighborhood orientation in both GLCM and HexGLCM.

As the amount of direction taken into account increases, the number of GLCMs naturally increases. While four GLCMs occur in the SIP domain, this number increases to six in the HIP domain. Figure 9 shows the HIP domain vertical counterpart of the image f given in Figure 8 and generated $HexGLCM_{0°}$, $HexGLCM_{30°}$, $HexGLCM_{60°}$, $HexGLCM_{90°}$, $HexGLCM_{120°}$, $HexGLCM_{150°}$, respectively.

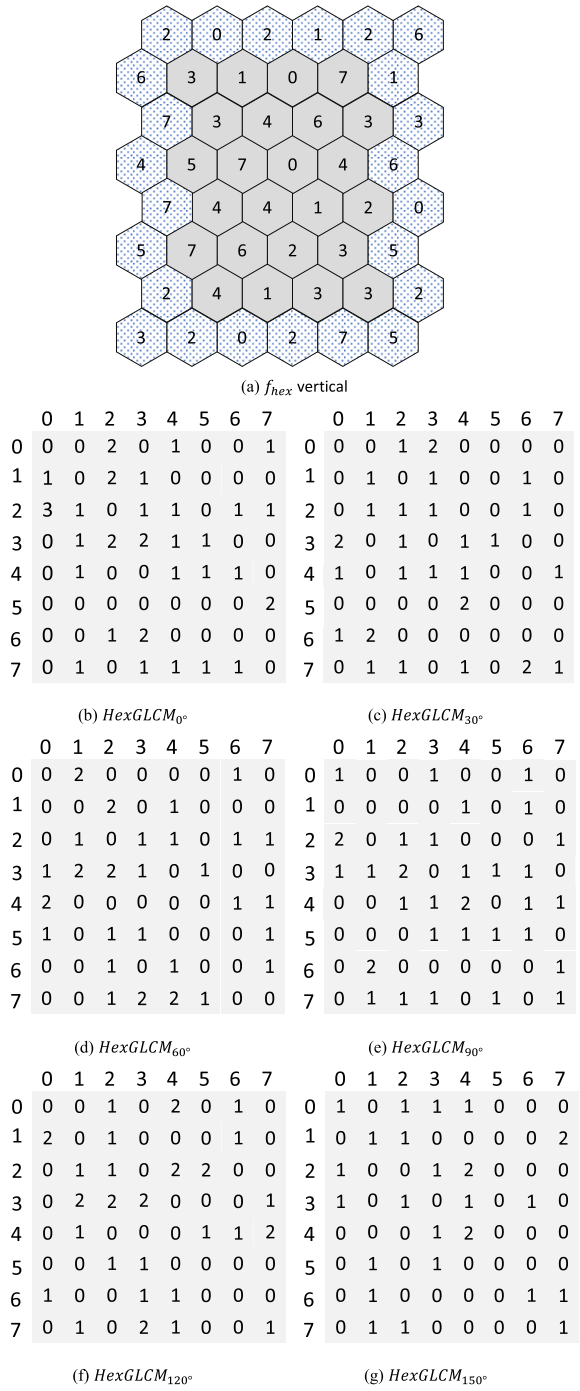

FIGURE 9. HIP vertical representation of image f and its corresponding HexGLCMs.

B. LBP - HexLBP

LBP's outstanding performance and little computing complexity have propelled it to the fore [49], [50], [51]. This

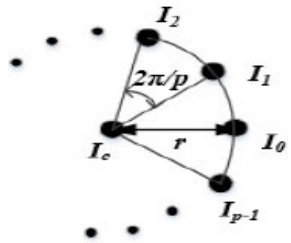

FIGURE 10. The p neighbors of the reference pixel I_c on the circle with radius r.

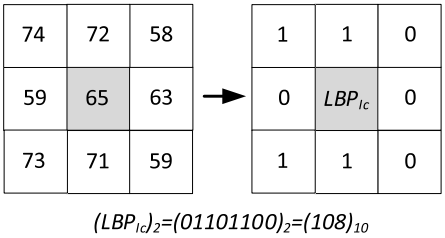

FIGURE 11. An example of the fundamental LBP being calculated.

section initially describes the fundamental SIP domain LBP before introducing the created HIP domain variant, HexLBP.

1) LBP

LBP's special identification rate and simplicity performance have attracted much attention and popularity [52]. It has affected many followers and served as a significant source for them; therefore, numerous research projects have been suggested as an extension of LBP. LBP was first created to classify textures. But once its strong performance was demonstrated, it has also been used to determine the connection between the pixels in images of faces [53], [54]. Additionally, a wide range of LBP versions has been put out to solve issues in a variety of domains, including object recognition [55], [56], motion and activity analysis [57], [58], biological image analysis [59], [60], visual inspection [61], etc. [3].

The original LBP expresses each pixel with a new gray-level value calculated concerning the nearby pixels' gray-level values in a 3 × 3 neighborhood to describe an image's spatial structure. Concatenating the single-digit binary values determined by comparing the reference pixel's magnitude with each neighbor yields a local binary value. Later, a more advanced version of this straightforward yet effective local pattern description technique emerged, giving rise to rotation invariance and multi-resolution analysis. The successor LBP operates on a circular neighborhood rather than the square pattern of the predecessor. The neighboring pixels settled equally apart from each other on a circle centered at the reference pixel (Figure 10) are considered during pattern description. Bilinear interpolation is used for regions where the circle does not pass through a particular pixel.

LBP of a reference pixel c is computed as follows, considering its P equally spaced neighbors on a circle of radius r:

$$LBP_{P,r}(c) = \sum_{P=0}^{P-1} s(I_c - I_p)2^P \tag{3}$$

where I_c and I_p denote the reference pixel's and the P^{th} surrounding pixel's intensity values, respectively. The binary digit's coefficient is identified by the function $s(x)$, which is defined as:

$$s(x) = \left\{ \begin{array}{l|l} 1 & if\ x \geq 0 \\ 0 & if\ x < 0 \end{array} \right\} \tag{4}$$

An exemplary demonstration of the basic LBP is given in Figure 11.

It is feasible to compute 2^p alternative patterns. The texture of the image ($I_{m\times n}$) is determined by considering the probability distributions of these LBP values on a histogram after each pixel's LBP values have been calculated as:

$$H(LBP_k) = \sum_{i=1}^{m} \sum_{j=1}^{n} \delta\{k, LBP(i,j)\} \tag{5}$$

where the Kroneck product function is indicated by $\delta\{k, LBP(i,j)\}$ [62].

Because each digit of the binary pattern corresponds to the outcome of comparing the intensity value of the reference pixel and the nearby pixel at the given direction, the LBP value of each pixel changes when the image is rotated. In other words, as the image is rotated, the specified neighbor's directional location likewise shifts, changing the position in the binary pattern that corresponds to it. It is suggested to create a rotation-invariant variation of the basic LBP. Some of the computed patterns have been found to have more information than others and to better capture the texture of the images. This group of 2^p patterns were referred to as uniform patterns by Ojala et al [63]. It is considered uniform if an LBP contains no more than two 0→1 or 1→0 transitions. While 10100100 and 00110011 are non-uniform, LBPs like 10011111 and 00010000 are uniform.

2) HEXLBP

Two versions of HexLBP are proposed, namely HexLBP_1 and HexLBP_2. In HexLBP_1, the six adjoin neighboring hexels (0°, 60°, 120°, 180°, 240°, 300°) laying on the one-hop tier are considered. However, in HexLBP_2, six more hexels laying on the angle directions 30°, 90°, 150°, 210°, 270°, and 330° are also additionally considered to improve texture discrimination. Figure 12 represents the orientations of HexLBP_1 and HexLBP_2.

In ordinary SIP domain LBP, since there are eight adjoint neighbors for each pixel, according to Eq. (3) $LBP_{P,r}(c)$ can take values between 0 and 255. In this interval, 58 uniform patterns are:

[0, 1, 2, 3, 4, 6, 7, 8, 12, 14, 15, 16, 24,
30, 31, 32, 48, 56, 60, 62, 63, 64, 96, 112, 120, 124, 126, 127,
129, 131, 135, 143, 159, 191, 192, 193, 195, 199, 207, 223,
225, 227, 231, 239, 240, 241, 243, 247, 248, 249, 251, 252,
253, 254, 255].

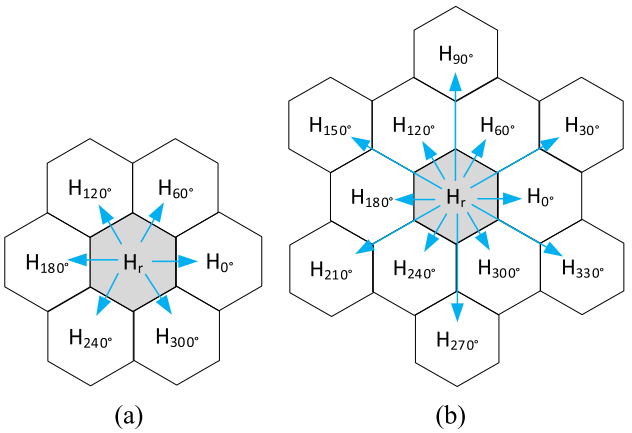

FIGURE 12. Angle-neighborhood orientation (a) HexLBP_1 (b) HexLBP_2.

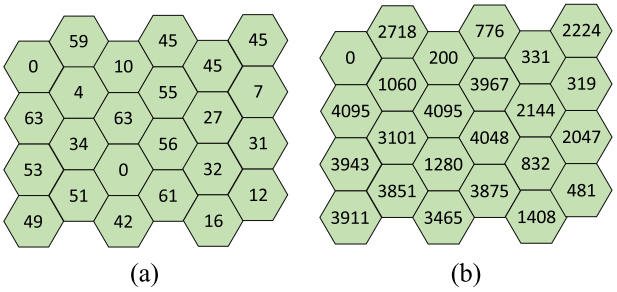

FIGURE 13. (a) HexLBP_1 (b) HexLBP_2.

However, this is different for HexLBP_1 and HexLBP_2. In HexLBP_1, there are six adjoint neighboring hexels for each hexel, and thus, $(HexLBP_1)_{P,r}(c)$ can take values between 0 and 63. In this interval, 22 uniform patterns are: [0, 1, 2, 3, 4, 6, 7, 8, 12, 14, 15, 16, 24, 28, 30, 31, 32, 48, 56, 60, 62, 63]. In HexLBP_2, twelve neighboring hexels of each hexel and thus, $(HexLBP_2)_{P,r}(c)$ can take values between 0 and 4095. In this interval, 134 uniform patterns are as shown in the equation at the bottom of the next page.

Figure 13 depicts the calculated HexLBP_1(f) and HexLBP_2(f). In HexLBP_1(f) and HexLBP_2(f), if the calculated new value of a hexel matches one of the members of the uniforms vector, the occurrence value of that value in the uniforms-occurrences-vector is incremented by one. Hence, the uniforms-occurrences-vector of HexLBP_1(f) and HexLBP_2(f) are as follows, respectively as shown in the equation at the bottom of the next page.

The last values of the vectors denote the count of the non-uniform values.

C. LHGPD – HEX LHGPD

Graphs are a typical structure with a long history. They have been used in the great majority of science and engineering fields aside from mathematics. In image processing and computer vision, graph theory may also be applied in various ways [64]. Graphs can be exploited to define representative descriptors to discriminate individuals' face images from each other. A graph-based face descriptor, LHGPD, and its hexagonal variant, HexLHGPD, are described in this section. First, LHGPD is briefly presented, and then HexLHGPD, its suggested hexagonal equivalent, is thoroughly detailed.

1) LHGPD

LHGPD [65] is a graph-based face descriptor that maintains its discriminating capacity even in settings with excessive noise, fluctuating facial expression, and uneven lighting exposure. In contrast to working directly on pixel values, face descriptor rendering is conducted on a graphical image representation in light of earlier successful uses of graphic theory in image processing. Thus, considering the intensity values and adjacencies of the pixels, an image is converted into a weighted directed graph. The produced directed graph's adjacency matrix is then created. The relevance of each vertex in the network, i.e., the associated pixel in the image, is stated by the centrality of each vertex, which is determined later. The final face descriptor is made up of these vertices' centrality values.

According to the proposed technique, a weighted and directed graph emerges from the image's alteration. A pixel beyond the image's boundaries has eight neighbors, which means it will always have eight incident edges that contact the corresponding vertex on the graph. As a result, such a pixel has a degree of eight, or $d(v_i) = 8$, where $d(v_i) = 8$, where $v_i \rightarrow g\left(I\left(p_{xy}\right)\right), x < nr\,(I)$ and $y < nc(I)$. This is $d(v_i) = 3$ for pixels close to the boundaries, i.e., $x = nr$ or $y = nc$. The transformation of a pixel $p(x, y)$ on an image $I_{nr\times nc}$ to a vertex v on the graph, G is represented by the $g()$ notation.

For a graph $G = (V, E)$, where $|E|$ denotes the total number of edges, the adjacency matrix A is $|E| \times |E|$. The adjacency matrix's components are described as follows:

$$A_{ij} = \left\{ \begin{array}{l} w_{ij}, e_i \in E \\ 0, otherwise \end{array} \right\} \tag{6}$$

$w_{ij} = 1$ by default, for an unweighted graph.

Since a pixel has no link to itself, the proposed method does not employ a loop on the graph representation of the image. As a result, the diagonal members of the adjacency matrix are all equal to zero. That is, $A_{ij} = 0$ if $i = j$.

An example SIP domain sub-image, its graph transformation, and the adjacency matrix of the created directed-weighted graph are shown in Figure 14.

An example sub-image is displayed in Figure 14(a). Each box has two triangles in it. The right triangle carries the pixel's intensity value, whereas the left triangle has the index number, which is also the vertex number in the graph. The pixels' immediate neighborhood and intensity values are considered when calculating the weights of the edges on the graph. As a result, there is an edge connection between each pixel's vertex and the vertex representing just its immediate neighbors. An edge's weight is equal to the difference between the densities of the vertex representing the low-density pixel and the vertex representing the

higher-density pixel, and it always has this orientation. The formula for the edge-weight computation is as follows:

$$w_{ij} = \left\{ \begin{array}{l} |p_i - p_j| + \varepsilon, i \neq j \\ 0, otherwise \end{array} \right\} \quad (7)$$

where ε stands for a number chosen between 0 and 1 to avoid confusion if the weight of an edge linking the vertices of two neighboring pixels with equal intensity values were set to zero. An edge weight of zero indicates the absence of a direct connection between these pixels. However, there is a connection between these pixels. Even if it has a very little non-zero value, this connection must be represented by an edge.

As is evident in Figure 14(b), the adjacency matrix of the image is a standard hollow matrix [66], as there are no loops and hence no elements on the diagonal. The adjacency matrix is also non-symmetric since the intensity-difference connection can only be stated in one direction.

Based on their locations in the image, pixels are divided into nine groups, as shown in Figure 15. Treating every pixel the same way is unreasonable since pixels in different groups have distinct adjacencies.

The significance of the edges and vertices in a graph is determined using centrality analysis, which has several applications in social networks and communication networks. There are several centrality measurements. To determine the significance of the edges and vertices in a graph, centrality analysis is employed, with applications ranging from communication networks to social networks. Up to this point, the most well-known and popular centrality measures are degree centrality, closeness centrality, outcloseness centrality, incloseness centrality, incloseness centrality, stress centrality, betweenness centrality, pagerank centrality, laplacian centrality [67], [68], [69], [70]. Degree centrality, which has two branches known as in-degree and out-degree centrality for directed graphs, is the count of vertex adjacencies on an undirected graph. The measure of a vertex's proximity to every other vertex on an undirected graph is called closeness centrality. Because the other vertices are closer to it, a vertex with a smaller total sum of distances is considered essential. On a directed network, outcloseness centrality is the sum of the distances from a specific vertex to all other accessible nodes. On a directed network, incloseness centrality is the sum of all distances from other nodes that can reach a given vertex. The quantity of shortest routes via a vertex in a directed graph is known as stress centrality. A vertex's relevance in the graph may be determined by how many shortcuts contain that vertex. Another shortest-paths-based measure used on both directed and undirected graphs is betweenness centrality. It expresses a vertex's control over the remainder of the network and is the normalized equivalent of stress centrality. Pagerank centrality is a system created by Google Co. and used on the World Wide Web to rank websites and web pages. Both directed and undirected graphs can use page ranking. Laplacian centrality may be used to quantify the impact of deactivating a node from a network [71], [72].

[0, 1, 2, 3, 4, 6, 7, 8, 12, 14, 15, 16, 24, 28, 30, 31, 32, 48,
56, 60, 62, 63, 64, 96, 112, 120, 124, 126, 127, 128, 192, 224, 240,
248, 252, 254, 255, 256, 384, 448, 480, 496, 504, 508, 510, 511,
512, 768, 896, 960, 992, 1008, 1016, 1020, 1022, 1023, 1024,
1536, 1792, 1920, 1984, 2016, 2032, 2040, 2044, 2046, 2047,
2048, 2049, 2051, 2055, 2063, 2079, 2111, 2175, 2303, 2559,
3071, 3072, 3073, 3075, 3079, 3087, 3103, 3135, 3199, 3327,
3583, 3584, 3585, 3587, 3591, 3599, 3615, 3647, 3711, 3839,
3840, 3841, 3843, 3847, 3855, 3871, 3903, 3967, 3968, 3969,
3971, 3975, 3983, 3999, 4031, 4032, 4033, 4035, 4039, 4047,
4063, 4064, 4065, 4067, 4071, 4079, 4080, 4081, 4083, 4087,
4088, 4089, 4091, 4092, 4093, 4094, 4095].

$\text{occ}(HexLBP_1(f)) = [2, 0, 0, 0, 1, 0, 1, 0, 1, 0, 0, 1, 0, 0, 0, 1, 1, 0, 1, 0, 0, 2, 13]$

$\text{occ}(HexLBP_2(f)) = [1, 0, 0, 0, 0, 0, 0, 0, 0, 0, 0, 0, 0, 0, 0, 0, 0, 0, 0, 0, 0, 0, 0, 0, 0, 0, 0, 0, 0, 0, 0, 0,$
$0, 0, 0, 0, 0, 0, 0, 0, 0, 0, 0, 0, 0, 0, 0, 0, 0, 0, 0, 0, 0, 0, 0, 0, 0, 0, 0, 0, 0, 0, 0, 0, 0, 0, 0, 0, 0, 0, 0, 0,$
$0, 0, 0, 0, 0, 0, 0, 0, 0, 0, 0, 0, 0, 0, 0, 0, 0, 0, 0, 0, 0, 0, 0, 0, 0, 0, 0, 0, 0, 0, 0, 0, 0, 0, 0, 0, 0, 0, 0, 0,$
$0, 0, 0, 0, 0, 1, 0, 0, 0, 0, 0, 0, 0, 0, 0, 0, 0, 0, 0, 0, 0, 0, 0, 0, 0, 0, 0, 0, 0, 0, 0, 0, 0, 0, 0, 0, 0, 0, 0, 0,$
$0, 2, 20]$

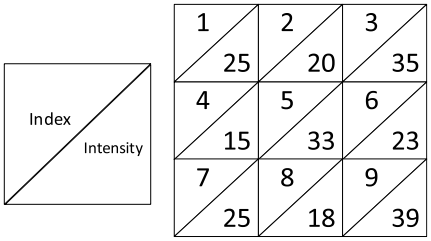

(a)

0	0	0	0	8	0	0	0	0
5	0	15	0	13	3	0	0	0
0	0	0	0	0	0	0	0	0
10	5	0	0	18	0	10	3	0
0	0	2	0	0	0	0	0	6
0	0	12	0	10	0	0	0	16
0	0	0	0	8	0	0	0	0
0	0	0	0	15	5	7	0	21
0	0	0	0	0	0	0	0	0

(b)

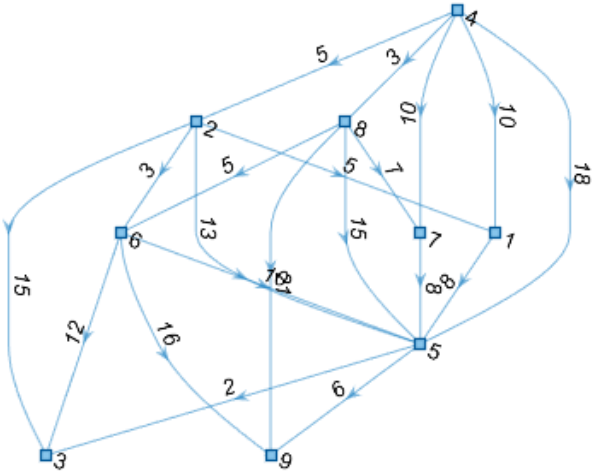

(c)

FIGURE 14. An example SIP domain (a) sample image, (b) adjacency matrix, and (c) weighted-directed-graph representation.

Since the resulting graph generated by LHGPD is directed, pagerank, incloseness, and outloseness metrics are implemented to evaluate the significance of each pixel in the picture. The graph's pagerank, proximity, and proximity rank analysis results in Figure 14(c) are shown in Table 2 for comparison.

2) HEXLHGPD

Since HexLHGPD is built on the hexagonal lattice logic, each hexel has six neighbors, not eight, unlike the SIP domain. This naturally reflects on the change in the graph representation of the image. Vertices corresponding to each hexel in the graph representation of the image are naturally linked to six vertices.

A HIP domain sub-image, its adjacency matrix, and graph transformation are illustrated in Figure 16.

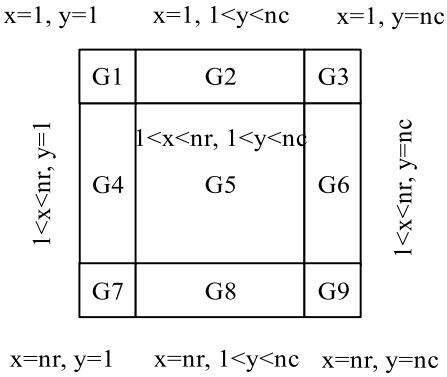

FIGURE 15. Division of an image's pixels into nine groups.

The total number of edges arising in the SIP domain is 20, but only 15 in the HIP domain, as can be observed when comparing Figures 14(c) and 16(c).

The graph's pagerank, proximity, and proximity rank analysis results in Figure 16(a) are shown in Table 3 for comparison.

IV. EXPERIMENTAL SETUP

A. DATASETS

Comprehensive simulations are run on five crucial and well-known datasets: CASPEAL-R1 [73], EXTENDED YALE B [74], FACES95 [75], ORL [76], and Lab2 [77] in order to analyze the performance of the HIP versions of the most fundamental SIP domain texture extraction algorithms. Simulations are done using MATLAB on the machine with 64 GB RAM and Intel Core i9-10900KF CPU @ 3.70 features.

The 30863 colorless images of 1040 people in the CAS-PEAL-R1 subset of the broader collection include folders emphasizing aging, expression, accessories, and lighting. While replicating these, lighting and emotion files (five images per participant) are considered. Each image has a resolution of 360 × 480. Sample images shown in Figure 17 depict how difficult it is to distinguish between them.

The EXTENDED YALE B dataset includes 16352360 × 480 resolution photos of 28 individuals in 9 distinct positions with 64 different illuminations. The EXTENDED YALE B dataset's images do not have any expression variation but considerable posture and lighting variations. Sample images show the EXTENDED YALE B dataset in Figure 18.

There are 72 people represented by 1440 colored 180 × 200 face images in the FACES95 dataset (male and female subjects). Images of the same subject show noticeable head (scale) and expression differences. Additionally, the artificial lighting setup causes significant lighting shifts on faces. Sample images from the FACES 95 dataset are shown in Figure 19. These images have exposure, expression, and illumination variations, all of which lower the performance of any face recognition technique.

The ORL dataset consists of 400112 × 92 pixel images from 40 different people. The images were taken at different

TABLE 2. Rank analysis results of the graph in Figure 14(c).

Vertex(v_i)-Pixel(p_i)	Page Rank	Out-closeness	In-closeness
$v_1 - p_1$	0.0733	0.0281	0.0313
v_2 - p_2	0.0605	0.0651	0.0156
v_3 - p_3	0.1854	0.0000	0.0696
v_4 - p_4	0.0517	0.0909	0.0000
v_5 - p_5	0.2327	0.0313	0.0938
v_6 - p_6	0.0774	0.0469	0.0352
v_7 - p_7	0.0733	0.0281	0.0313
v_8 - p_8	0.0605	0.0651	0.0156
v_9 - p_9	0.1854	0.0000	0.0696

TABLE 3. Rank analysis results of the graph in Figure 16(c).

Vertex(v_i)-Hexel(h_i)	Page Rank	Out-closeness	In-closeness
$v_1 - h_1$	0.1036	0.0000	0.0313
v_2 - h_2	0.0808	0.0500	0.0156
v_3 - h_3	0.1736	0.0000	0.0558
v_4 - h_4	0.0690	0.0851	0.0000
v_5 - h_5	0.1461	0.0313	0.0625
v_6 - h_6	0.0690	0.0469	0.0000
v_7 - h_7	0.1036	0.0000	0.0313
v_8 - h_8	0.0808	0.0500	0.0156
v_9 - h_9	0.1736	0.0000	0.0558

times with various lighting conditions and facial expressions. Sample images from the ORL dataset are shown in Figure 20.

The HITSZ Lab2 dataset collected and released by the Harbin Institute of Technology includes 2000 facial images, each 200 × 200, from participants. These images were taken in various lighting situations, including natural light, natural light+left light, natural light+right light, and natural light+right light+left right. The images also show significant changes in facial expression and posture [78].

B. MODEL TRAINING

Face recognition is a primary classification task. Two ways can be followed in this classification process. The first is the binary classification method, which works with the logic of one vs. all. In this, a classifier model is developed, utilizing supervised training for each person, hence the class. After training a classifier for a person, to determine which person a new image belongs to, one can ask all the classifiers individually and find out to whom it belongs. The other method is developing a single model to classify multi-label. In this, a label is assigned to each person, and after the model is trained, the new image is given to the classifier as an input, and the person it belongs to is obtained from the class information. In this study, we preferred this method, namely the multi-label classification method.

Optimizable Discriminant Analysis (ODA), Optimizable Ensemble (OE), and Optimizable Neural Network (ONN) structure that the MATLAB Classification Learner Wizard

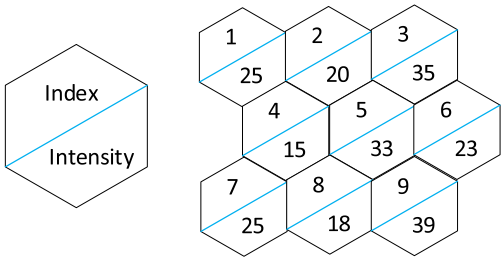

(a)

0	0	0	0	0	0	0	0	0
5	0	15	0	13	0	0	0	0
0	0	0	0	0	0	0	0	0
10	5	0	0	18	0	10	3	0
0	0	2	0	0	0	0	0	6
0	0	12	0	10	0	0	0	16
0	0	0	0	0	0	0	0	0
0	0	0	0	15	0	7	0	21
0	0	0	0	0	0	0	0	0

(b)

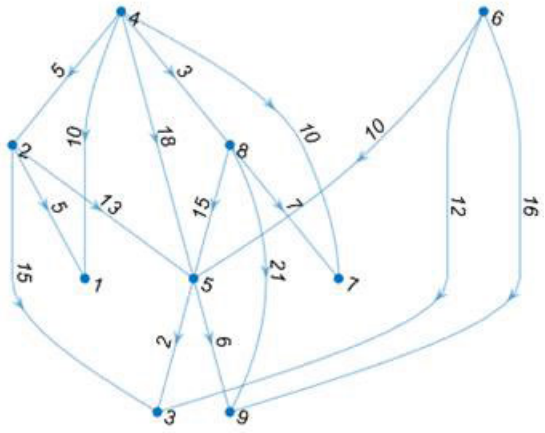

(c)

FIGURE 16. An example HIP domain (a) sample image, (b) adjacency matrix and (c) weighted-directed-graph representation.

FIGURE 17. Samples of subject images taken from the CAS-PEAL-R1 dataset.

provides are used during the training stage. The reason for utilizing the optimization is mainly that hyperparameters can significantly impact the performance of a model. We used the hyperparameter optimization feature in the Classification Learner app to automate the selection of hyperparameter values rather than manually picking and testing these

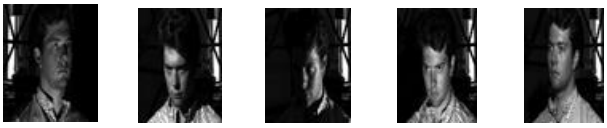

FIGURE 18. Samples of subject images taken from the EXTENDED YALE B dataset.

FIGURE 19. Samples of subject images taken from the FACES 95 dataset.

FIGURE 20. Samples of subject images taken from the ORL dataset.

TABLE 4. The terminology used in simulations and their corresponding description.

Term	Description
HF_glcm0_Sq	Haralick Texture Features for 0° on SIP
HF_glcm45_Sq	Haralick Texture Features for 45° on SIP
HF_glcm90_Sq	Haralick Texture Features for 90° on SIP
HF_glcm135_Sq	Haralick Texture Features for 135° on SIP
HF_glcm04590135_Sq	Concatanted Haralick Texture Features of 0°, 45°, 90°, and 135° on SIP
HF_glcm0_Hex	Haralick Texture Features for 0° on HIP
HF_glcm30_Hex	Haralick Texture Features for 30° on HIP
HF_glcm60_Hex	Haralick Texture Features for 60° on HIP
HF_glcm90_Hex	Haralick Texture Features for 90° on HIP
HF_glcm120_Hex	Haralick Texture Features for 120° on HIP
HF_glcm150_Hex	Haralick Texture Features for 150° on HIP
HF_glcm060120_Hex	Concatanted Haralick Texture Features of 0°, 60°, and 120° on HIP
HF_glcm0306090120150_Hex	Concatanted Haralick Texture Features of 0°, 30°, 60°, 90°, 120°, and 150° on HIP
LBP_Hex	Local Binary Pattern on HIP
LBP_Hex_Ext	Extended Local Binary Pattern on HIP
LBP_Sq	Local Binary Pattern on SIP
LHGPD_Hex	LHGPD on HIP
LHGPD_Sq	LHGPD on SIP

parameters. Using an optimization approach to reduce the model classification error, the app explores various combinations of hyperparameter values for a given model type. It then returns a model with optimized hyperparameters.

Before training the model, the entire datasets are partitioned into train and test portions in the ratio of 80% and 20%, respectively. 5-fold cross-validation is applied to protect the models against overfitting.

V. RESULTS AND DISCUSSION

This study proposes the HIP domain counterparts of some texture descriptors of the SIP domain and clarifies their facial recognition performances on the fundamental face datasets. Eighteen feature sets are generated for each dataset.

TABLE 5. The recognition accuracy performances on The CASPEALR1 dataset.

Term	ODA	OE	ONN
HF_glcm0_Sq	0.7792	0.8600	0.7800
HF_glcm45_Sq	0.8700	0.8375	0.7875
HF_glcm90_Sq	0.7969	0.8600	0.8000
HF_glcm135_Sq	0.8281	0.8325	0.7775
HF_glcm04590135_Sq	0.8900	0.8875	0.9200
HF_glcm0_Hex	0.8000	0.8175	0.7875
HF_glcm30_Hex	0.8281	0.8400	0.8125
HF_glcm60_Hex	0.8125	0.8350	0.7750
HF_glcm90_Hex	0.8400	0.8425	0.8050
HF_glcm120_Hex	0.8500	0.8500	0.7750
HF_glcm150_Hex	0.8250	0.8275	0.8200
HF_glcm060120_Hex	0.8675	0.8900	0.8700
HF_glcm0306090120150_Hex	0.8900	0.9150	0.9100
LBP_Hex	0.8900	0.8000	0.8275
LBP_Hex_Ext	0.9500	0.8400	0.9425
LBP_Sq	0.9400	0.8300	0.8950
LHGPD_Hex	**0.8900**	**0.8675**	**0.9625**
LHGPD_Sq	0.9281	0.8825	0.9500

TABLE 6. The recognition accuracy performances on the FACES95 dataset.

Term	ODA	OE	ONN
HF_glcm0_Sq	0.9160	0.9357	0.9500
HF_glcm45_Sq	0.8760	0.8750	0.8893
HF_glcm90_Sq	0.8423	0.8482	0.8750
HF_glcm135_Sq	0.8840	0.8714	0.9000
HF_glcm04590135_Sq	0.9420	0.9286	0.9589
HF_glcm0_Hex	0.9184	0.8982	0.9500
HF_glcm30_Hex	0.8967	0.8929	0.9125
HF_glcm60_Hex	0.8802	0.8714	0.8857
HF_glcm90_Hex	0.8898	0.8661	0.9214
HF_glcm120_Hex	0.8681	0.8732	0.8786
HF_glcm150_Hex	0.9097	0.8929	0.9161
HF_glcm060120_Hex	0.9429	0.9357	0.9786
HF_glcm0306090120150_Hex	**0.9931**	**0.9625**	**0.9714**
LBP_Hex	0.8750	0.8286	0.9161
LBP_Hex_Ext	0.9388	0.8875	0.9500
LBP_Sq	0.8700	0.8714	0.9375
LHGPD_Hex	0.9517	0.9446	0.9571
LHGPD_Sq	0.9329	0.9429	0.9429

The terminology and corresponding descriptions are given in Table 4. The facial recognition accuracy results on the CASPEALR1 dataset are given in Table 5.

Table 6 shows the facial recognition accuracy results on the FACES95 dataset. Table 7 shows the facial recognition accuracy results on the EXTENDED YALE B dataset.

Table 8 shows the facial recognition accuracy results on the Lab2 dataset. Table 9 shows the facial recognition accuracy results on the ORL dataset.

EXTENDED YALE B is the dataset that performs the best across all face descriptors. This is because EXTENDED YALE B has excessive face images per user or class. On the contrary, the lowest accuracy performance was obtained in Lab2 compared to other datasets. This is because the dataset consists of facial images of Chinese participants with various lighting and facial expressions.

As stated at the beginning of the article, the performances of the original SIP versions of GLCM, LBP, and LHGPD

TABLE 7. The recognition accuracy performances on the extended YALE B dataset.

Term	ODA	OE	ONN
HF_glcm0_Sq	0.8988	0.8651	0.8998
HF_glcm45_Sq	0.8484	0.8502	0.8810
HF_glcm90_Sq	0.8444	0.8452	0.8522
HF_glcm135_Sq	0.8952	0.9087	0.8770
HF_glcm04590135_Sq	0.9592	0.9405	0.9603
HF_glcm0_Hex	0.9032	0.8929	0.9008
HF_glcm30_Hex	0.8833	0.8571	0.8591
HF_glcm60_Hex	0.8675	0.8313	0.8839
HF_glcm90_Hex	0.8556	0.8373	0.8532
HF_glcm120_Hex	0.8506	0.8502	0.8591
HF_glcm150_Hex	0.8992	0.8502	0.8621
HF_glcm060120_Hex	0.9151	0.8968	0.9454
HF_glcm0306090120150_Hex	0.9270	0.9688	0.9653
LBP_Hex	0.8756	0.8929	0.9444
LBP_Hex_Ext	0.9214	0.9653	0.9931
LBP_Sq	0.9619	0.9683	0.9851
LHGPD_Hex	**0.9931**	**0.9950**	**0.9990**
LHGPD_Sq	0.9960	0.9931	0.9970

TABLE 8. The recognition accuracy performances on the LAB2 dataset.

Term	ODA	OE	ONN
HF_glcm0_Sq	0.5150	0.5950	0.7200
HF_glcm45_Sq	0.5612	0.7000	0.5950
HF_glcm90_Sq	0.6150	0.6950	0.5963
HF_glcm135_Sq	0.5900	0.6963	0.7550
HF_glcm04590135_Sq	0.9200	0.7188	0.8550
HF_glcm0_Hex	0.5175	0.7000	0.5750
HF_glcm30_Hex	0.5800	0.6900	0.7563
HF_glcm60_Hex	0.5862	0.6638	0.8013
HF_glcm90_Hex	0.6000	0.7000	0.8050
HF_glcm120_Hex	0.5750	0.6850	0.7838
HF_glcm150_Hex	0.5800	0.7150	0.7788
HF_glcm060120_Hex	0.8500	0.7150	0.8125
HF_glcm0306090120150_Hex	0.9700	0.9100	0.9000
LBP_Hex	0.6575	0.7088	0.7950
LBP_Hex_Ext	0.8100	0.7800	0.8700
LBP_Sq	0.8250	0.8050	0.8150
LHGPD_Hex	**0.9725**	**0.8888**	**0.9750**
LHGPD_Sq	0.9000	0.8988	0.9600

is compared to those of the HIP domain counterparts. Naturally, the GLCM04590135, which concatenates the Haralick Feature sets of 0°, 45°, 90°, and 135°s, gets the maximum accuracy if we search for the SIP domain versions of GLCM. If we look at the HIP domain variants of GLCM, GLCM03060901201250, which is the concatenated version of the Haralick Feature feature sets of 0°, 30°, 60°, 90°, 120°, and 150°s, achieves the most remarkable accuracy rate. This is due to the feature set's inclusion of additional unique elements.

Regarding LBP, each pixel has eight neighbors in the SIP domain and 6 in the HIP domain. This is reflected in the variety of uniform patterns. While there are 59 uniform patterns due to 8 neighborhood 8 bits in SIP domain LBP, there are 23 uniform patterns due to 6 bits in HIP domain LBP. This naturally reflects in performance. As the tables show, SIP domain LBP achieves a higher success rate than HIP domain LBP. More neighbors are considered in LBP Hex Ext since

TABLE 9. The recognition accuracy performances on the ORL dataset.

Term	ODA	OE	ONN
HF_glcm0_Sq	0.8194	0.8194	0.8299
HF_glcm45_Sq	0.8889	0.8194	0.8715
HF_glcm90_Sq	0.8924	0.8056	0.8889
HF_glcm135_Sq	0.8750	0.8333	0.8611
HF_glcm04590135_Sq	0.9821	0.9028	0.9583
HF_glcm0_Hex	0.8611	0.9028	0.8750
HF_glcm30_Hex	0.9097	0.8229	0.9167
HF_glcm60_Hex	0.8924	0.8368	0.8889
HF_glcm90_Hex	0.9271	0.8576	0.8472
HF_glcm120_Hex	0.9028	0.8611	0.8750
HF_glcm150_Hex	0.9167	0.8194	0.8333
HF_glcm060120_Hex	0.9722	0.8611	0.9167
HF_glcm0306090120150_Hex	0.9882	0.8889	0.9444
LBP_Hex	0.7778	0.7917	0.8542
LBP_Hex_Ext	0.7500	0.9062	0.9444
LBP_Sq	0.7535	0.8299	0.9028
LHGPD_Hex	**0.9444**	**0.9028**	**0.9861**
LHGPD_Sq	0.8507	0.8917	0.9340

the neighborhood wall is more extended, which inevitably broadens the variability of the uniform pattern. There are 135 uniform patterns. This is, of course, the single element that improves performance.

LHGPD is a high-performance face descriptor, which achieves the highest face description performance among the other mentioned methods, as clarified by the simulation results. It can exhibit high-performance face discrimination even on the most challenging dataset, LAB2. The HIP domain performs better here likewise than the SIP domain LHGPD. This is because each pixel's neighbors in the HIP domain are spaced equally apart, and as a result, their impacts are also equally spaced out.

VI. CONCLUSION

This study presents HIP versions of the most basic texture extraction studies in SIP, namely Gray-Level-Co-occurrence-Matrices (GLCM), Local Binary Pattern (LBP), and our recent work, local-holistic graph-based descriptor (LHGPD). According to the experiment findings, GLCM, LBP, and LHGPD in the HIP domain perform on par with and occasionally outperform their SIP domain equivalents regarding face recognition accuracy. This is because the effects of each pixel's neighbors in the HIP domain are uniformly spaced apart.

This field, which looks promising for future studies, is aimed to transform and even develop the SIP domain face recognition methods into the HIP domain.

DECLARATION OF COMPETING INTEREST

The authors declare that they have no known competing financial interests or personal relationships that could have appeared to influence the work reported in this paper.

DATA AVAILABILITY

Data sharing does not apply to this article, as no new datasets were generated or analyzed during the current study.

REFERENCES

[1] S. Biswas and J. Sil, "An efficient face recognition method using contourlet and curvelet transform," *J. King Saud Univ.-Comput. Inf. Sci.*, vol. 32, no. 6, pp. 718–729, Jul. 2020, doi: 10.1016/j.jksuci.2017.10.010.

[2] R. Jafri and H. R. Arabnia, "A survey of face recognition techniques," *J. Inf. Process. Syst.*, vol. 5, no. 2, pp. 41–68, Jun. 2009, doi: 10.3745/JIPS.2009.5.2.041.

[3] N. Cevik and T. Cevik, "DLGBD: A directional local gradient based descriptor for face recognition," *Multimedia Tools Appl.*, vol. 78, no. 12, pp. 15909–15928, Jun. 2019, doi: 10.1007/s11042-018-6967-4.

[4] N. Ullah, A. Javed, M. Ali Ghazanfar, A. Alsufyani, and S. Bourouis, "A novel DeepMaskNet model for face mask detection and masked facial recognition," *J. King Saud Univ.-Comput. Inf. Sci.*, vol. 34, no. 10, pp. 9905–9914, Nov. 2022, doi: 10.1016/j.jksuci.2021.12.017.

[5] J. S. Nayak and M. Indiramma, "An approach to enhance age invariant face recognition performance based on gender classification," *J. King Saud Univ.-Comput. Inf. Sci.*, vol. 34, no. 8, pp. 5183–5191, Sep. 2022, doi: 10.1016/j.jksuci.2021.01.005.

[6] T. Cevik and N. Cevik, "RIMFRA: Rotation-invariant multi-spectral facial recognition approach by using orthogonal polynomials," *Multimedia Tools Appl.*, vol. 78, no. 18, pp. 26537–26567, Sep. 2019, doi: 10.1007/s11042-019-07816-6.

[7] Z. Xu, Y. Jiang, Y. Wang, Y. Zhou, W. Li, and Q. Liao, "Local polynomial contrast binary patterns for face recognition," *Neurocomputing*, vol. 355, pp. 1–12, Aug. 2019, doi: 10.1016/j.neucom.2018.09.056.

[8] Z. Wang, Z. Miao, Q. M. Jonathan Wu, Y. Wan, and Z. Tang, "Low-resolution face recognition: A review," *Vis. Comput.*, vol. 30, no. 4, pp. 359–386, Apr. 2014, doi: 10.1007/s00371-013-0861-x.

[9] Z. Lei, M. Pietikainen, and S. Z. Li, "Learning discriminant face descriptor," *IEEE Trans. Pattern Anal. Mach. Intell.*, vol. 36, no. 2, pp. 289–302, Feb. 2014, doi: 10.1109/TPAMI.2013.112.

[10] J. Lu, V. E. Liong, X. Zhou, and J. Zhou, "Learning compact binary face descriptor for face recognition," *IEEE Trans. Pattern Anal. Mach. Intell.*, vol. 37, no. 10, pp. 2041–2056, Oct. 2015, doi: 10.1109/TPAMI.2015.2408359.

[11] W. Zhao, R. Chellappa, P. J. Phillips, and A. Rosenfeld, "Face recognition," *ACM Comput. Surveys*, vol. 35, no. 4, pp. 399–458, Dec. 2003, doi: 10.1145/954339.954342.

[12] S. Z. Li and A. K. Jain, *Handbook of Face Recognition*. London, U.K.: Springer, 2011, doi: 10.1007/978-0-85729-932-1.

[13] N. Çevik and T. Çevik, "A novel high-performance holistic descriptor for face retrieval," *Pattern Anal. Appl.*, vol. 23, no. 1, pp. 371–383, Feb. 2020, doi: 10.1007/s10044-019-00803-5.

[14] R. M. Haralick, "Statistical and structural approaches to texture," *Proc. IEEE*, vol. 67, no. 5, pp. 786–804, May 1979, doi: 10.1109/PROC.1979.11328.

[15] R. M. Haralick, K. Shanmugam, and I. Dinstein, "Textural features for image classification," *IEEE Trans. Syst., Man, Cybern.*, vol. SMC-3, no. 6, pp. 610–621, Nov. 1973, doi: 10.1109/TSMC.1973.4309314.

[16] M. Turk and A. Pentland, "Eigenfaces for recognition," *J. Cognit. Neurosci.*, vol. 3, no. 1, pp. 71–86, Jan. 1991, doi: 10.1162/jocn.1991.3.1.71.

[17] X. Wang and X. Tang, "A unified framework for subspace face recognition," *IEEE Trans. Pattern Anal. Mach. Intell.*, vol. 26, no. 9, pp. 1222–1228, Sep. 2004, doi: 10.1109/TPAMI.2004.57.

[18] P. N. Belhumeur, J. P. Hespanha, and D. J. Kriegman, "Eigenfaces vs. Fisherfaces: Recognition using class specific linear projection," *IEEE Trans. Pattern Anal. Mach. Intell.*, vol. 19, no. 7, pp. 711–720, Jul. 1997, doi: 10.1109/34.598228.

[19] P. Comon, "Independent component analysis, a new concept?" *Signal Process.*, vol. 36, no. 3, pp. 287–314, Apr. 1994, doi: 10.1016/0165-1684(94)90029-9.

[20] X. He, S. Yan, Y. Hu, P. Niyogi, and H.-J. Zhang, "Face recognition using laplacianfaces," *IEEE Trans. Pattern Anal. Mach. Intell.*, vol. 27, no. 3, pp. 328–340, Mar. 2005, doi: 10.1109/TPAMI.2005.55.

[21] N. Cevik, T. Cevik, and A. GurhanlI, "Novel multispectral face descriptor using orthogonal Walsh codes," *IET Image Process.*, vol. 13, no. 7, pp. 1097–1104, May 2019, doi: 10.1049/iet-ipr.2018.6423.

[22] S. Murala, R. P. Maheshwari, and R. Balasubramanian, "Local tetra patterns: A new feature descriptor for content-based image retrieval," *IEEE Trans. Image Process.*, vol. 21, no. 5, pp. 2874–2886, May 2012, doi: 10.1109/TIP.2012.2188809.

[23] M. Yang, L. Zhang, S. C.-K. Shiu, and D. Zhang, "Monogenic binary coding: An efficient local feature extraction approach to face recognition," *IEEE Trans. Inf. Forensics Security*, vol. 7, no. 6, pp. 1738–1751, Dec. 2012, doi: 10.1109/TIFS.2012.2217332.

[24] T. Mohammad and M. L. Ali, "Robust facial expression recognition based on local monotonic pattern (LMP)," in *Proc. 14th Int. Conf. Comput. Inf. Technol. (ICCIT)*, Dec. 2011, pp. 572–576, doi: 10.1109/ICCITechn.2011.6164854.

[25] X. Tan and B. Triggs, "Enhanced local texture feature sets for face recognition under difficult lighting conditions," *IEEE Trans. Image Process.*, vol. 19, no. 6, pp. 1635–1650, Jun. 2010, doi: 10.1109/TIP.2010.2042645.

[26] B. Zhang, Y. Gao, S. Zhao, and J. Liu, "Local derivative pattern versus local binary pattern: Face recognition with high-order local pattern descriptor," *IEEE Trans. Image Process.*, vol. 19, no. 2, pp. 533–544, Feb. 2010, doi: 10.1109/TIP.2009.2035882.

[27] T. Jabid, M. H. Kabir, and O. Chae, "Local directional pattern (LDP) for face recognition," in *Proc. Dig. Tech. Papers Int. Conf. Consum. Electron. (ICCE)*, Jan. 2010, pp. 329–330, doi: 10.1109/ICCE.2010.5418801.

[28] T. Jabid and O. Chae, "Local transitional pattern: A robust facial image descriptor for automatic facial expression recognition," in *Proc. Int. Conf. Comput. Converg. Technol.*, 2011, pp. 33–44.

[29] S. Yang and B. Bhanu, "Facial expression recognition using emotion Avatar image," in *Proc. IEEE Int. Conf. Autom. Face Gesture Anal.*, Mar. 2011, pp. 866–871, doi: 10.1109/FG.2011.5771364.

[30] S. Liu, Y. Zhang, and K. Liu, "Facial expression recognition under partial occlusion based on Weber local descriptor histogram and decision fusion," in *Proc. 33rd Chin. Control Conf.*, Jul. 2014, pp. 4664–4668, doi: 10.1109/ChiCC.2014.6895725.

[31] M. S. Islam, "Local gradient pattern—A novel feature representation for facial expression recognition," *J. AI Data Mining*, vol. 2, no. 1, pp. 33–38, 2014, doi: 10.22044/JADM.2014.147.

[32] A. Hafiane, G. Seetharaman, and B. Zavidovique, *Median Binary Pattern for Textures Classification* (Lecture Notes in Computer Science), M. Kamel and A. Campilho, Eds. Berlin, Germany: Springer, 2007, pp. 387–398, doi: 10.1007/978-3-540-74260-9_35.

[33] M. S. Islam and S. Auwatanamo, "Facial expression recognition using local arc pattern," *Trends Appl. Sci. Res.*, vol. 9, no. 2, pp. 113–120, Feb. 2014, doi: 10.3923/tasr.2014.113.120.

[34] M. Varma and A. Zisserman, "A statistical approach to material classification using image patch exemplars," *IEEE Trans. Pattern Anal. Mach. Intell.*, vol. 31, no. 11, pp. 2032–2047, Nov. 2009, doi: 10.1109/TPAMI.2008.182.

[35] S. Lazebnik, C. Schmid, and J. Ponce, "A sparse texture representation using local affine regions," *IEEE Trans. Pattern Anal. Mach. Intell.*, vol. 27, no. 8, pp. 1265–1278, Aug. 2005, doi: 10.1109/TPAMI.2005.151.

[36] T. Ahonen, A. Hadid, and M. Pietikainen, "Face recognition with local binary patterns," in *Computer Vision—ECCV* (Lecture Notes in Computer Science), T. Pajdla and J. Matas, Eds. Berlin, Germany: Springer, 2004, pp. 469–481, doi: 10.1007/978-3-540-24670-1_36.

[37] Q. Yin and J.-N. Kim, "Rotation-invariant texture classification using circular Gabor wavelets based local and global features," *Chin. J. Electron.*, vol. 17, no. 4, pp. 646–648, 2008.

[38] J. Melendez, M. A. Garcia, and D. Puig, "Efficient distance-based per-pixel texture classification with Gabor wavelet filters," *Pattern Anal. Appl.*, vol. 11, nos. 3–4, pp. 365–372, Sep. 2008, doi: 10.1007/s10044-007-0097-3.

[39] K. Jafari-Khouzani and H. Soltanian-Zadeh, "Radon transform orientation estimation for rotation invariant texture analysis," *IEEE Trans. Pattern Anal. Mach. Intell.*, vol. 27, no. 6, pp. 1004–1008, Jun. 2005, doi: 10.1109/TPAMI.2005.126.

[40] T. C. Hales, "Cannonballs and honeycombs," *Notices-Amer. Math. Soc.*, vol. 47, no. 4, pp. 440–449, 2000.

[41] T. C. Hales, "The honeycomb conjecture," *Discrete Comput. Geometry*, vol. 25, no. 1, pp. 1–22, Jan. 2001, doi: 10.1007/s004540010071.

[42] S. Coleman, B. Scotney, and B. Gardiner, "Processing hexagonal images in a virtual environment," in *Image Analysis and Processing—ICIAP* (Lecture Notes in Computer Science), P. Foggia, C. Sansone, and M. Vento, Eds. Berlin, Germany: Springer, 2009, pp. 920–928, doi: 10.1007/978-3-642-04146-4_98.

[43] J. D. Allen, "Perfect reconstruction filter banks for the hexagon grid," in *Proc. 5th Int. Conf. Inf. Commun. Signal Process.*, 2005, pp. 73–76, doi: 10.1109/ICICS.2005.1689007.

[44] L. Wang, X. He, R. Du, W. Jia, Q. Wu, and W. Yeh, "Facial expression recognition on hexagonal structure using LBP-based histogram variances," in *Advances in Multimedia Modeling* (Lecture Notes in Computer Science), K.-T. Lee, W.-H. Tsai, H.-Y. M. Liao, T. Chen, J.-W. Hsieh, and C.-C. Tseng, Eds. Berlin, Germany: Springer, 2011, pp. 35–45, doi: 10.1007/978-3-642-17829-0_4.

[45] D. Zhang, X. Zhang, L. Li, and H. Liu, "Face recognition via sparse representation of SIFT feature on hexagonal-sampling image," in *Proc. 9th Int. Conf. Graphic Image Process. (ICGIP)*, Apr. 2018, p. 238, doi: 10.1117/12.2304894.

[46] A. Azeem, M. Sharif, J. H. Shah, and M. Raza, "Hexagonal scale invariant feature transform (H-SIFT) for facial feature extraction," *J. Appl. Res. Technol.*, vol. 13, no. 3, pp. 402–408, Jun. 2015, doi: 10.1016/j.jart.2015.07.006.

[47] N. Cevik, T. Cevik, O. Osman, A. Gurhanli, S. Nematzadeh, and F. Sahin, "Improved exploiting modification direction steganography for hexagonal image processing," *J. King Saud Univ.-Comput. Inf. Sci.*, vol. 34, no. 10, pp. 9273–9283, Nov. 2022, doi: 10.1016/j.jksuci.2022.09.007.

[48] N. Cevik, "Face recognition by grey-level co-occurrence matrices in hexagonal digital image processing," *Turkish Stud.-Inf. Technol. Appl. Sci.*, vol. 14, no. 2, pp. 149–165, 2019, doi: 10.29228/TurkishStudies.22825.

[49] T. Ojala, M. Pietikäinen, and D. Harwood, "A comparative study of texture measures with classification based on featured distributions," *Pattern Recognit.*, vol. 29, no. 1, pp. 51–59, Jan. 1996, doi: 10.1016/0031-3203(95)00067-4.

[50] T. Ojala, M. Pietikainen, and T. Maenpaa, "Multiresolution gray-scale and rotation invariant texture classification with local binary patterns," *IEEE Trans. Pattern Anal. Mach. Intell.*, vol. 24, no. 7, pp. 971–987, Jul. 2002, doi: 10.1109/TPAMI.2002.1017623.

[51] M. Pietikäinen, T. Ojala, and Z. Xu, "Rotation-invariant texture classification using feature distributions," *Pattern Recognit.*, vol. 33, no. 1, pp. 43–52, 2000, doi: 10.1016/S0031-3203(99)00032-1.

[52] L. Nanni, S. Brahnam, S. Ghidoni, E. Menegatti, and T. Barrier, "Different approaches for extracting information from the co-occurrence matrix," *PLoS ONE*, vol. 8, no. 12, Dec. 2013, Art. no. e83554, doi: 10.1371/journal.pone.0083554.

[53] S. Chakraborty, S. K. Singh, and P. Chakraborty, "Local gradient hexa pattern: A descriptor for face recognition and retrieval," *IEEE Trans. Circuits Syst. Video Technol.*, vol. 28, no. 1, pp. 171–180, Jan. 2018, doi: 10.1109/TCSVT.2016.2603535.

[54] T. Ahonen, A. Hadid, and M. Pietikainen, "Face description with local binary patterns: Application to face recognition," *IEEE Trans. Pattern Anal. Mach. Intell.*, vol. 28, no. 12, pp. 2037–2041, Dec. 2006, doi: 10.1109/TPAMI.2006.244.

[55] R. Lienhart and J. Maydt, "An extended set of Haar-like features for rapid object detection," in *Proc. Int. Conf. Image Process.*, 2010, pp. 37–43. [Online]. Available: http://cmp.felk.cvut.cz/cvww2010/cvww2010-proceedings.pdf

[56] A. Satpathy, X. Jiang, and H.-L. Eng, "LBP-based edge-texture features for object recognition," *IEEE Trans. Image Process.*, vol. 23, no. 5, pp. 1953–1964, May 2014, doi: 10.1109/TIP.2014.2310123.

[57] G. Zhao and M. Pietikainen, "Dynamic texture recognition using local binary patterns with an application to facial expressions," *IEEE Trans. Pattern Anal. Mach. Intell.*, vol. 29, no. 6, pp. 915–928, Jun. 2007, doi: 10.1109/TPAMI.2007.1110.

[58] P. A. Crook, V. Kellokumpu, G. Zhao, and M. Pietikainen, "Human activity recognition using a dynamic texture based method," in *Proc. Brit. Mach. Vis. Conf.*, 2008, p. 88, doi: 10.5244/C.22.88.

[59] L. Nanni, A. Lumini, and S. Brahnam, "Local binary patterns variants as texture descriptors for medical image analysis," *Artif. Intell. Med.*, vol. 49, no. 2, pp. 117–125, Jun. 2010, doi: 10.1016/j.artmed.2010.02.006.

[60] L. Nanni, S. Brahnam, and A. Lumini, "A local approach based on a local binary patterns variant texture descriptor for classifying pain states," *Exp. Syst. Appl.*, vol. 37, no. 12, pp. 7888–7894, Dec. 2010, doi: 10.1016/j.eswa.2010.04.048.

[61] O. Silven, M. Niskanen, and H. Kauppinen, "Wood inspection with non-supervised clustering," *Mach. Vis. Appl.*, vol. 13, nos. 5–6, pp. 275–285, Mar. 2003, doi: 10.1007/s00138-002-0084-z.

[62] B. Yang and S. Chen, "A comparative study on local binary pattern (LBP) based face recognition: LBP histogram versus LBP image," *Neurocomputing*, vol. 120, pp. 365–379, Nov. 2013, doi: 10.1016/j.neucom.2012.10.032.

[63] T. Ojala, M. Pietikainen, and T. Maenpaa, "Gray scale and rotation invariant texture classification with local binary patterns," in *Computer Vision—ECCV* (Lecture Notes in Computer Science), D. Vernon, Ed. Dublin, Ireland: Springer, 2000, pp. 404–420, doi: 10.1007/3-540-45054-8_27.

[64] O. Lezoray and L. Grady, *Image Processing and Analysis With Graphs: Theory and Practice*. Boca Raton, FL, USA: CRC Press, 2012, doi: 10.1201/b12281.

[65] T. Cevik, N. Cevik, and M. Zontul, "A local-holistic graph-based descriptor for facial recognition," *Multimedia Tools Appl.*, vol. 82, no. 13, pp. 19275–19298, May 2023, doi: 10.1007/s11042-022-14152-9.

[66] J. E. Gentle, *Matrix Algebra*. New York, NY, USA: Springer, 2007, doi: 10.1007/978-0-387-70873-7.

[67] J. Kepner and J. Gilbert, *Graph Algorithms in the Language of Linear Algebra*. Philadelphia, PA, USA: Society for Industrial and Applied Mathematics, 2011, doi: 10.1137/1.9780898719918.

[68] J. Liu, Q. Xiong, W. Shi, X. Shi, and K. Wang, "Evaluating the importance of nodes in complex networks," *Phys. A, Stat. Mech. Appl.*, vol. 452, pp. 209–219, Jun. 2016, doi: 10.1016/j.physa.2016.02.049.

[69] Y. Hui, L. Zun, and L. Yong-Jun, "Key nodes in complex networks identified by multi-attribute decision-making method," *Acta Phys. Sinica*, vol. 62, no. 2, 2013, Art. no. 020204, doi: 10.7498/aps.62.020204.

[70] C. Gao, D. Wei, Y. Hu, S. Mahadevan, and Y. Deng, "A modified evidential methodology of identifying influential nodes in weighted networks," *Phys. A, Stat. Mech. Appl.*, vol. 392, no. 21, pp. 5490–5500, Nov. 2013, doi: 10.1016/j.physa.2013.06.059.

[71] M. Newman, *Networks*. Oxford, U.K.: Oxford Univ. Press, 2010, doi: 10.1093/acprof:oso/9780199206650.001.0001.

[72] X. Qi, E. Fuller, Q. Wu, Y. Wu, and C.-Q. Zhang, "Laplacian centrality: A new centrality measure for weighted networks," *Inf. Sci.*, vol. 194, pp. 240–253, Jul. 2012, doi: 10.1016/j.ins.2011.12.027.

[73] W. Gao, B. Cao, S. Shan, X. Chen, D. Zhou, X. Zhang, and D. Zhao, "The CAS-PEAL large-scale Chinese face database and baseline evaluations," *IEEE Trans. Syst., Man, Cybern. A, Syst. Humans*, vol. 38, no. 1, pp. 149–161, Jan. 2008, doi: 10.1109/TSMCA.2007.909557.

[74] A. S. Georghiades, P. N. Belhumeur, and D. J. Kriegman, "From few to many: Illumination cone models for face recognition under variable lighting and pose," *IEEE Trans. Pattern Anal. Mach. Intell.*, vol. 23, no. 6, pp. 643–660, Jun. 2001, doi: 10.1109/34.927464.

[75] D. L. Spacek. (2008). *Computer Vision Science Research Projects*. Accessed: Dec. 1, 2022. [Online]. Available: www.essex.ac.uk/mv/allfaces/faces95.html

[76] AL Cambridge. *The Database of Faces*. Accessed: Jan. 31, 2023. [Online]. Available: https://cam-orl.co.uk/facedatabase.html

[77] Y. Xu, "Bimodal biometrics based on a representation and recognition approach," *Opt. Eng.*, vol. 50, no. 3, Mar. 2011, Art. no. 037202, doi: 10.1117/1.3554740.

[78] K. Guo, S. Wu, and Y. Xu, "Face recognition using both visible light image and near-infrared image and a deep network," *CAAI Trans. Intell. Technol.*, vol. 2, no. 1, pp. 39–47, Mar. 2017, doi: 10.1016/j.trit.2017.03.001.

TANER CEVIK received the B.Sc. degree in computer engineering from Istanbul Technical University, Istanbul, in 2001, and the Ph.D. degree from Istanbul University, in 2012. He joined the Department of Computer Engineering, Istanbul Arel University, in 2023, where he is currently a Professor. His research interests include image processing, machine learning, and wireless communications.

NAZIFE CEVIK received the Ph.D. degree from Istanbul University, in 2015. She joined the Computer Engineering Department, Istanbul Arel University, in 2015, where she is currently an Associate Professor. Her research interests include image processing, machine learning, and bioinformatics.

JAWAD RASHEED (Member, IEEE) received the B.S. degree in telecommunication engineering from the National University of Computer and Emerging Sciences, Pakistan, and the M.S. degree in electrical and electronics engineering and the Ph.D. degree in computer engineering.

He is currently an Assistant Professor with the Department of Software Engineering, İstanbul Nişantaşi University, Istanbul, Turkey. He is the author/coauthor of more than 50 papers published in well-reputed journals and highly ranked conferences. His research interests include artificial intelligence, image processing, pattern recognition, the IoT, and data analytics. He was a gold medalist and awarded the Academic Excellence Award for securing straight A's in O' Level exams held by Cambridge University. Later, he also received a prestigious Doctorate and Research Scholarship for his Ph.D. studies (for three years). He serves as the Guest/Lead-Guest/Topic Editor for Special Issues of the *Symmetry*, *Mathematics*, *Healthcare*, *Applied Sciences*, *Electronics*, *Healthcare*, and *Journal of Sensor and Actuator Networks*. Recently, he served as a book Editor for *Lecture Notes on Data Engineering and Communications Technologies—Forthcoming Networks and Sustainability in the IoT Era* (Springer). In addition, he is the General Chair of IEEE ICAIoT and IEEE FoNeS-AIoT and chairs the technical program committee of Springer FoNeS-IoT 2021.

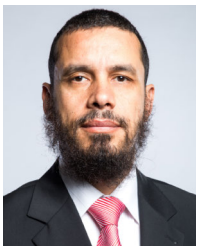

ADNAN M. ABU-MAHFOUZ (Senior Member, IEEE) received the M.Eng. and Ph.D. degrees in computer engineering from the University of Pretoria. He is currently a Chief Researcher and the Centre Manager of the Emerging Digital Technologies for 4IR (EDT4IR) Research Centre, Council for Scientific and Industrial Research (CSIR), an Extraordinary Professor with the University of Pretoria, a Professor Extraordinaire with the Tshwane University of Technology, and a Visiting Professor with the University of Johannesburg. His research interests include wireless sensor and actuator networks, low power wide area networks, software defined wireless sensor networks, cognitive radio, network security, network management, and sensor/actuator node development. He is the Section Editor-in-Chief of the *Journal of Sensor and Actuator Networks*, an Associate Editor of IEEE Access, IEEE Internet of Things, and IEEE Transaction on Industrial Informatics, and a member of many IEEE technical communities.

ONUR OSMAN received the B.Sc. degree from the Electrical Engineering Department, Istanbul Technical University, in 1994, and the M.Sc. and Ph.D. degrees, in 1998 and 2004, respectively. He is currently the Dean of the Engineering Faculty, İstanbul Topkapi University. His research interests include image and signal processing, artificial intelligence, biomedical signals and systems, game intelligence, neuroscience, machine learning, deep learning, and optimization. He founded various research and development departments and acted as a research and development coordinator in universities.